Supplementary Material to "Spin-triplet superconductivity in Weyl nodal-line semimetals"

(Dated: February 13, 2022)

In this Supplementary Material, we present experimental details regarding the synthesis, the physical-properties characterization, as well as the data analysis of LaNiSi, LaPtSi, and LaPtGe noncentrosymmetric superconductors. We also provide additional details on the computation of the electronic specific heat using the Bogoliubov-de-Gennes formalism for the minimal two-band model in the internally antisymmetric nonunitary triplet (INT) state.

Supplementary Note 1

Crystal structure. The phase purity and crystal structure of LaNiSi, LaPtSi, and LaPtGe 111 materials were checked via powder x-ray diffraction (XRD) at room temperature. As shown in Supplementary Figure 1, the XRD patterns of LaNiSi and LaPtSi are well indexed by a noncentrosymmetric body-centered tetragonal crystal structure with a space group $I4_1md$ (No. 109). The refinement of LaPtGe is shown in Fig. 1 in the main text, where the crystal structure of the unit cell is also reported. The refined lattice parameters and atomic coordinates are summarized in Supplementary Table 1 and are consistent with those reported previously [1–3]. Tiny amount of extra phases ($< 4\%$) were identified in LaNiSi and LaPtSi. Such extra phases can be indexed as La_5Si_3 in LaNiSi, while no match with reported phases was found in LaPtSi [see arrows in Supplementary Figure 1(b)]. We recall that La_5Si_3 behaves as a simple metal which does not undergo any phase transition down to 2 K [4]. Finally, no extraneous phases could be detected in LaPtGe.

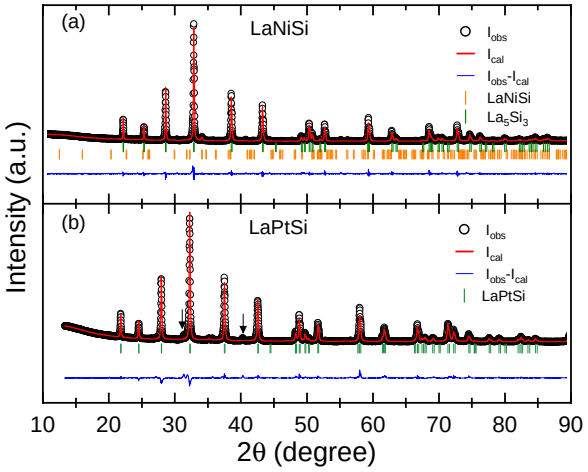

Supplementary Figure 1. Rietveld refinements of the room-temperature powder x-ray diffraction patterns for LaNiSi (a) and LaPtSi (b). The Rietveld refinements of LaPtGe can be found in the main text. Black circles show the experimental data, while red lines the refined profiles. Ticks below the patterns indicate the Bragg-peak reflections, while blue lines show the residues.

Supplementary Note 2

Zero-field electrical resistivity. The temperature dependence of the electrical resistivity $\rho(T)$, collected in zero field from 0.3 K to 300 K, reveals the metallic character of LaNiSi, LaPtSi, and LaPtGe [see Supplementary Figure 2(a)]. The electrical resistivity in the low-T region (below 10 K) is shown in Supplementary Figure 2(b). Here, the superconducting transition, with onset temperature $T_c^{onset} = 1.35$ K and zero-resistivity temperature $T_c^{zero} = 1.25$ K, is clearly visible for LaNiSi. While for LaPtSi and LaPtGe, the $T_c^{onset} =$ 3.65 and 3.6 K, $T_c^{zero} = 3.5$ and 3.3 K, respectively. The T_c values determined from the electrical-resistivity measurements are consistent with those determined from magnetic susceptibility- and heat-capacity measurements (see Figs. 1 and 6 in the main text). The T_c values determined from $\chi(T)$, $C(T)/T$, and $\rho(T)$ are summarized in Supplementary Table 5. A sharp superconducting transition with $\Delta T \sim 0.1 - 0.3$ K indicates the good sample quality of all the investigated 111 materials. By extending the electrical resistivity to zero temperature, the derived residual resistivities are $\rho_0 \sim 18$, 62, and 66 $\mu\Omega$cm for LaNiSi, LaPtSi, and LaPtGe, respectively.

Supplementary Table 1. Refined lattice parameters and atomic coordinates of LaNiSi, LaPtSi, and LaPtGe (all sharing the $I4_1md$ space group).

LaNiSi ($a = b = 4.1781$ Å, $c = 14.0657$ Å)

Atom	Wyckoff position	x	y	z
La	4a	0.00000	0.00000	0.58306
Ni	4a	0.00000	0.00000	0.17214
Si	4a	0.00000	0.00000	0.00618

LaPtSi ($a = b = 4.2465$ Å, $c = 14.5148$ Å)

Atom	Wyckoff position	x	y	z
La	4a	0.00000	0.00000	0.59495
Pt	4a	0.00000	0.00000	0.18085
Si	4a	0.00000	0.00000	0.01095

LaPtGe ($a = b = 4.2665$ Å, $c = 14.9553$ Å)

Atom	Wyckoff position	x	y	z
La	4a	0.00000	0.00000	0.58962
Pt	4a	0.00000	0.00000	0.17431
Ge	4a	0.00000	0.00000	0.00727

Supplementary Note 3

Determination of lower critical field H_{c1}. To perform transverse-field (TF) μSR measurements in a superconductor, the applied magnetic field should exceed the lower critical field H_{c1}, so that the additional field-distribution broadening due to the flux-line lattice (FFL) can be quantified from the muon-spin relaxation rate, the latter being directly related to the magnetic penetration depth. As shown in Supplementary Figure 3(a)-(c), to determine H_{c1}, the field-dependent mag-

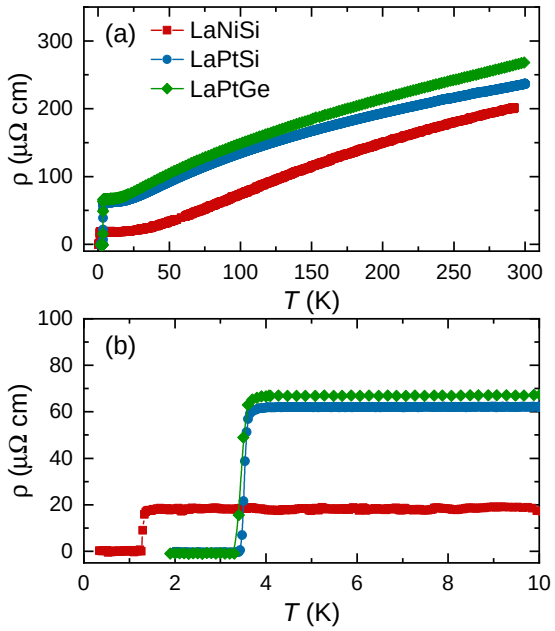

Supplementary Figure 2. (a) Temperature-dependent electrical resistivity $\rho(T)$ for LaNiSi, LaPtSi, and LaPtGe. The enlarged plots of low-T resistivity are shown in panel (b), where the superconducting transition can be clearly identified. The T_c values determined from $\rho(T)$ are consistent with those determined from $\chi(T)$ and $C(T)/T$.

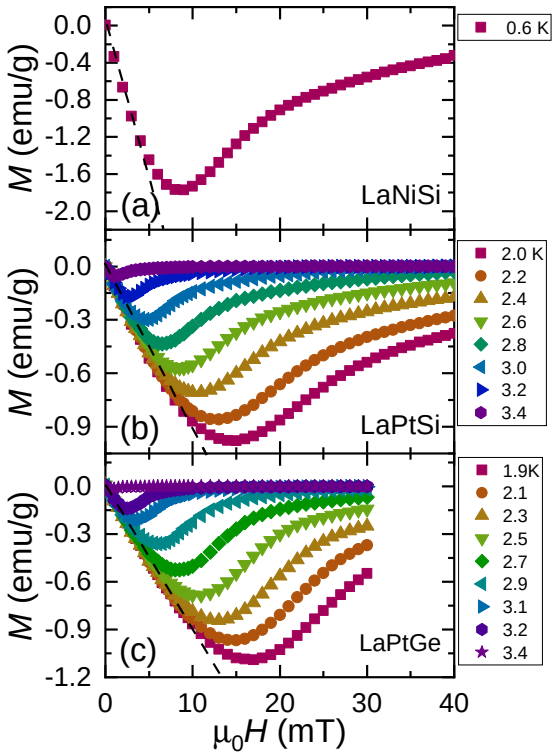

Supplementary Figure 3. Field-dependent magnetization recorded at various temperatures up to T_c for LaNiSi (a), LaPtSi (b), and LaPtGe (c). For each temperature, as indicated by the dashed lines, H_{c1} was determined as the value where $M(H)$ starts deviating from linearity.

netization was measured at various temperatures up to T_c. The estimated H_{c1} values are plotted in Fig. 2 in the main text as a function of temperature for LaNiSi, LaPtSi, and LaPtGe, respectively. The estimated lower critical fields $\mu_0 H_{c1}(0)$ = 3.9(5), 9.6(2), and 11.8 (1) mT for LaNiSi, LaPtSi, and LaPtGe, respectively. The H_{c1} values determined from the magnetization data are consistent with the values calculated from magnetic penetration depth measured by TF-μSR.

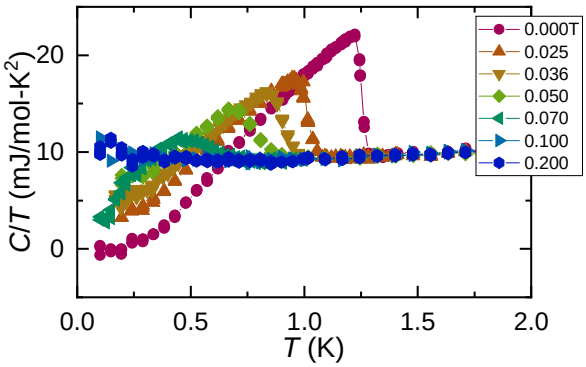

Supplementary Figure 4. Temperature dependence of the specific heat measured in various applied magnetic fields up to 0.2 T for LaNiSi.

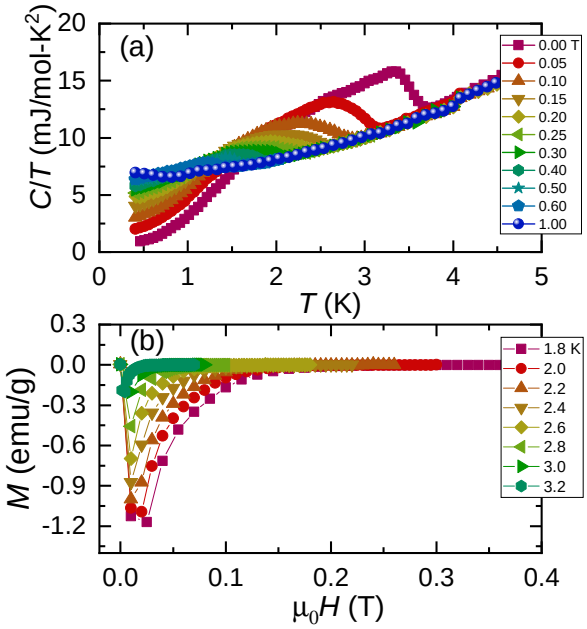

Supplementary Figure 5. (a) Temperature dependence of specific heat, measured under various magnetic fields up to 1 T and (b) field-dependent magnetization measured at various temperatures up to T_c for LaPtSi.

Supplementary Note 4

Determination of the upper critical field H_{c2}. To calculate the penetration depth from the measured muon-spin relaxation rate, we determined first the upper critical fields H_{c2} of 111 materials by measuring their bulk properties, including the temperature-dependent specific heat $C(T,H)/T$ in various magnetic fields and the field-dependent magnetization $M(H,T)$ at various temperatures, up to T_c.

As shown in Supplementary Figure 4(a), in LaNiSi we detect a zero-field superconducting transition at $T_c \sim 1.25$ K from $C(T)/T$ data, corresponding to the temperature where

electrical resistivity drops to zero (see Supplementary Figure 2). The specific-heat anomaly at T_c shifts to lower temperature with increasing magnetic field. The derived upper critical fields H_{c2} versus the reduced temperature T/T_c are summarized in Fig. 2(d) in the main text. For LaNiSi, $H_{c2}(T)$ is well described by the Werthamer-Helfand-Hohenberg (WHH) model [5], which gives $\mu_0 H_{c2}^{WHH}(0) = 0.10(1)$ T. In the LaPtGe case, the field-dependent magnetization at various temperatures, $M(H,T)$, was also measured to track H_{c2}. In the $M(H,T)$ plot, the diamagnetic signal disappears once the applied magnetic field exceeds the upper critical field [Supplementary Figure 6(b)]. The H_{c2} values determined from magnetization measurements are highly consistent with those determined from heat-capacity measurements [see Fig. 2(f) in the main text]. Similar to LaNiSi, the $H_{c2}(T)$ of LaPtGe is also well described by the WHH model, leading to $\mu_0 H_{c2}^{WHH}(0) = 0.44(1)$ T.

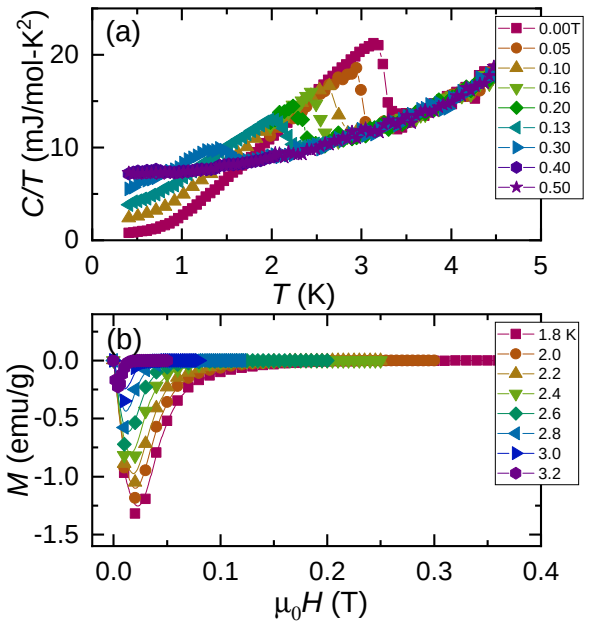

Supplementary Figure 6. (a) Temperature dependence of specific heat, measured in magnetic fields up to 0.5 T and (b) field dependence of magnetization measured at various temperatures up to T_c for LaPtGe.

The temperature-dependent specific heat in various magnetic fields and the field-dependent magnetization at various temperatures were also measured for LaPtSi (see Supplementary Figure 5). In contrast to LaNiSi and LaPtGe, in LaPtSi [see Fig. 2(e) in main text], both WHH and Ginzburg-Landau (GL) models can reasonably reproduce $H_{c2}(T)$ at low fields, i.e., $\mu_0 H_{c2} < 0.2$ T. However, at higher magnetic fields, both models deviate significantly from the experimental data and underestimate the H_{c2} values. Such a discrepancy most likely hints at multiple superconducting gaps in LaPtSi, as evidenced also by the positive curvature of $H_{c2}(T)$, a typical feature of multigap superconductors. The $H_{c2}(T)$ of LaPtSi exhibits clear kinks close to 0.2 T. The two-band model shows remarkable agreement with the experimental data and provides $\mu_0 H_{c2}(0) = 1.17(2)$ T for LaPtSi [6]. However, note that, due to similar gap sizes (or to small relative weights), such multigap features are not distinct in the superfluid density or in the zero-field electronic specific heat, requiring further investigations.

In the GL theory of superconductivity, the magnetic penetration depth λ is related to the coherence length ξ, and the lower critical field via $\mu_0 H_{c1} = (\Phi_0/4\pi\lambda^2)[\ln(\kappa)+\alpha(\kappa)]$, where $\Phi_0 = 2.07\times10^{-3}$ T μm^2 is the quantum of magnetic flux, $\kappa = \lambda/\xi$ is the GL parameter, and $\alpha(\kappa)$ is a parameter which converges to 0.497 for $\kappa \gg 1$ [7]. Due to the small κ value, here α was fixed at 0.12. By using $\mu_0 H_{c1}$ and ξ values [calculated from $\mu_0 H_{c2}(0) = \Phi_0/2\pi\xi(0)^2$], the resulting λ_{GL} is compatible with the experimental value determined from μSR data. A GL parameter $\kappa > 1$ confirms again that LaNiSi, LaPtSi, and LaPtGe are type-II superconductors. All the superconducting parameters are summarized in Supplementary Table 5.

Supplementary Note 5

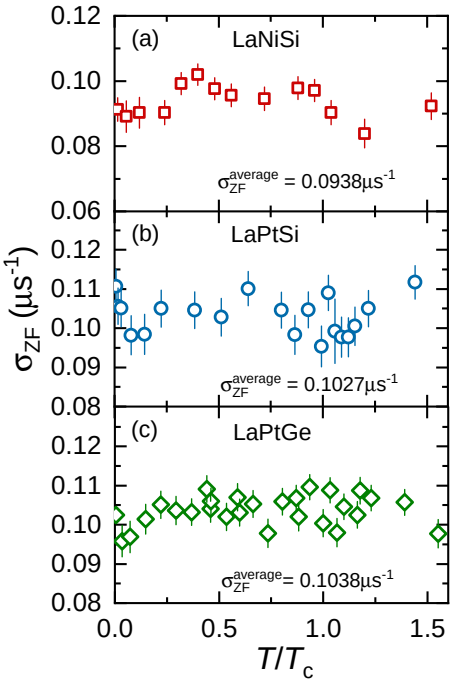

Supplementary Figure 7. Nuclear-related Gaussian relaxation rates σ_{ZF} derived from ZF-μSR vs. reduced temperature T/T_c for LaNiSi (a), LaPtSi (b), and LaPtGe (c), respectively. While $\sigma_{ZF}(T)$ is almost temperature independent, $\Lambda_{ZF}(T)$ (of electronic nature) shows a weak but clear increase in the superconducting state (see main text).

Zero-field μSR. The ZF-μSR data were analyzed by a combined Lorentzian and Gaussian Kubo-Toyabe relaxation function [see details in Eq. (2) in the main text]. As can be seen in Supplementary Figure 7, the derived Gaussian relaxation rates $\sigma_{ZF}(T)$ (of nuclear origin) exhibit a weak temperature dependence with no clear anomaly across T_c for all the samples. As shown in Supplementary Figure 7(a), (b), and (c), the average σ_{ZF} values turn out to be 0.0938, 0.1027, and 0.1038 μs^{-1} for LaNiSi, LaPtSi, and LaPtGe, respectively. The comparable Gaussian relaxation rates reflect the similar nuclear magnetic moments in 111 materials. The ZF-μSR data shown in the main text were analyzed by fixing σ_{ZF}s to their respective average values. A small yet clear increase below T_c was observed in the $\Lambda_{ZF}(T)$ channel, indicating the presence of spontaneous magnetic fields and thus, the

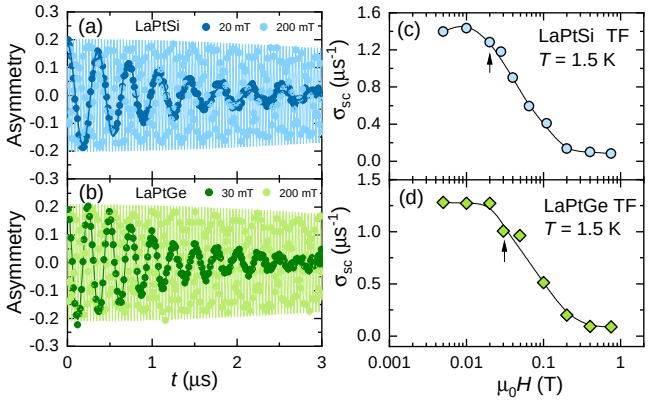

Supplementary Figure 8. TF-μSR spectra for LaPtSi (a) and LaPtGe (b) collected at various applied magnetic fields at 1.5 K (i.e., in the superconducting state). The superconducting Gaussian relaxation rates σ_{sc} vs. external field for LaPtSi (c) and LaPtGe (d). The arrows indicate the applied field value chosen for the temperature-dependent TF-μSR measurements. The solid lines are guides to the eyes.

breaking of time-reversal symmetry (TRS) in the superconducting state of these 111 materials (see Fig. 3 in the main text).

Supplementary Note 6

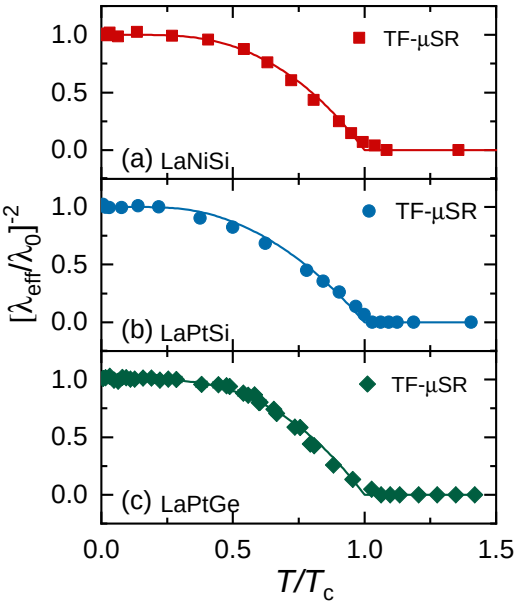

Supplementary Figure 9. Superfluid density vs. reduced temperature T/T_c for LaNiSi (a), LaPtSi (b), and LaPtGe (c). Lines represent fits to an *s*-wave model in the dirty-limit case. The derived gap values are summarized in Supplementary Table 5.

Transverse-field μSR. To investigate the superconducting properties of 111 materials at a microscopic level, we carried out transverse-field (TF)-μSR measurements in an applied magnetic field down to 0.02 K. The optimal field values for TF-μSR experiments were determined via preliminary field-dependent μSR relaxation-rate measurements at 1.5 K (see Supplementary Figure 8). All the magnetic fields were applied above T_c, and the TF-μSR spectra were collected

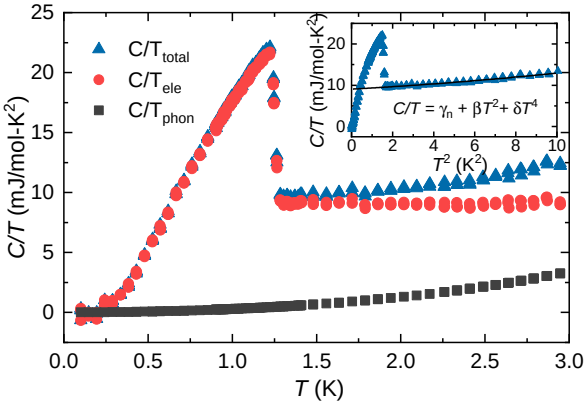

Supplementary Figure 10. Temperature dependence of the zero-field total, electronic, and phononic specific heat of LaNiSi. The inset shows the C/T versus T^2, where the solid line is a fit to $C/T = \gamma_n + \beta T^2 + \delta T^4$.

after a field-cooling process. Representative TF-μSR spectra collected at 20 and 200 mT are shown in Supplementary Figure 8(a) and (b) for LaPtSi and LaPtGe, respectively. The solid lines represent fits using again the model described by Eq. (3) in the main text. As shown in Supplementary Figure 8(c) and (d), the resulting superconducting Gaussian relaxation rates $\sigma_{sc}(H)$ exhibits a clear decrease above 10 and 20 mT for LaPtSi and LaPtGe, respectively, which are close to their lower critical field values H_{c1} (see Supplementary Table 5 below). By considering the decrease of intervortex distance with field and the vortex-core effects, a field of 20 (LaPtSi) and 30 mT (LaPtGe) (indicated by the arrows) was chosen for the temperature-dependent TF-μSR study. Similar to LaPtSi and LaPtGe, in LaNiSi a field of 15 mT, twice the $\mu_0 H_{c1}(0)$ value, was chosen for the temperature-dependent study.

For the 111 materials studied here, the estimated BCS coherence length ξ_0 is larger than the electronic mean-free path l_e ($\xi_0/l_e \sim 1.6$–4) (see details in Supplementary Table 5). Therefore, similar to previous studies [8, 9], they are close to the dirty limit. Unlike in the clean-limit case ($\xi_0 \ll l_e$) [see Eq. (5) in the main text], in the BCS approximation, the temperature dependent superfluid density in the dirty limit is given by [10]:

$$\rho_{sc}(T) = \frac{\Delta(T)}{\Delta_0} \tanh\left[\frac{\Delta(T)}{2k_B T}\right], \qquad (1)$$

where $\Delta(T)$ is the same as in the main text. The solid lines in Supplementary Figure 9 are fits to the above model. For all the above 111 materials, ξ_0 and l_e are not significantly different and exhibit similar magnitudes. Hence, both the clean- and the dirty-limit models describe quite well the low-T superfluid density, and yield similar superconducting gaps (see Supplementary Table 5).

Supplementary Note 7

Specific-heat measurements. Since the specific heat in the superconducting state offers valuable insight into the superconducting gap and its symmetry, the zero-field specific heat data were further analyzed (see Fig. 5 in the main text).

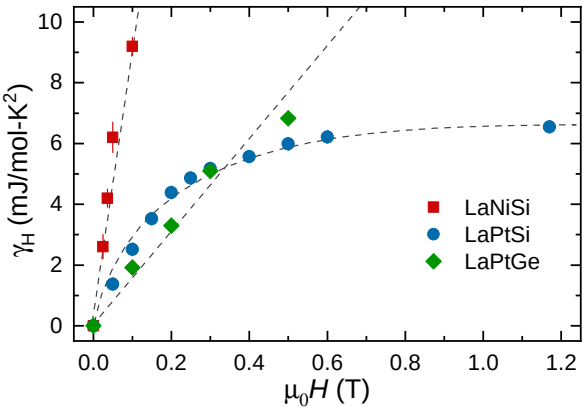

Supplementary Figure 11. Electronic specific heat coefficient γ_H vs applied magnetic field for LaNiSi, LaPtSi, and LaPtGe. For a given field, γ_H is obtained as the linear extrapolation of C/T vs T^2 in the superconducting state to zero temperature. The dashed-lines are guides to the eyes.

As an example, here we show how to obtain the electronic specific heat from the measured specific-heat data for LaNiSi. The same method was used to extract the electronic specific heat of LaPtSi and LaPtGe. Supplementary Figure 10 shows the temperature dependence of the total, electronic, and phononic specific heat of LaNiSi measured in zero field. To subtract the phonon contribution from the measured specific heat, the normal-state specific-heat data were fitted to the expression $C/T = \gamma_n + \beta T^2 + \delta T^4$, where γ_n is the normal-state electronic specific-heat coefficient, whereas β and δ are the phonon specific-heat coefficients [11]. The solid line in the inset of Supplementary Figure 10 is a fit to the above expression. The phonon contribution can hence be calculated using the expression, $C/T_{phon} = \beta T^2 + \delta T^4$, which is then subtracted from the raw experimental data. The resulting $C/T_{ele} = C/T_{total} - C/T_{phon}$ curve (shown with red symbols in Supplementary Figure 10), represents the electronic specific heat. The estimated electronic and phononic specific-heat coefficients for the considered 111 materials are summarized in Supplementary Table 5.

In LaPtSi, since the weight of the second gap might be relatively small (and the gap sizes are not significantly different), it is difficult to discriminate between a single- and a two-gap superconductor based on the temperature-dependent superfluid density or zero-field electronic specific heat data. Yet, the two-gap feature of LaPtSi is clearly reflected in its upper critical field $H_{c2}(T)$ [see Fig. 2(e) in the main text]. Since normally the different gaps respond differently to an external field, $H_{c2}(T)$ exhibits different features in a two-gap superconductor compared to a single-gap superconductor.

The multigap nature of LaPtSi was further confirmed by the field-dependent electronic specific heat coefficient $\gamma_H(H)$. The plots of γ_H vs the applied magnetic field are shown in Supplementary Figure 11 for all the three cases. For LaNiSi and LaPtGe, $\gamma_H(H)$ show a clear linear field dependence expected for fully-gapped superconductors with a single gap, similar to other single-gap superconductors, e.g., $Re_{0.82}Nb_{0.18}$ [12]. While for LaPtSi, $\gamma_H(H)$ clearly deviates from the linear field dependence, or from the square-root dependence $\sqrt{H}$, the latter being expected for nodal superconductors [13, 14]. LaPtSi, instead, exhibits similar features to other well known multigap superconductors, as e.g.,

Supplementary Table 2. Important basis functions of the C_{4v} point group for its two-dimensional irreducible representation E in case of strong SOC. Here, A_1, A_2, and B_2 are constants, independent of k.

C_{4v}	Basis functions	
Irreps	Scalar (even)	Vector (odd)
E	$A_1 k_z \begin{pmatrix} k_x \\ k_y \end{pmatrix}$	$\begin{pmatrix} A_2 k_z \hat{x} + B_2 k_x \hat{z} \\ A_2 k_z \hat{y} + B_2 k_y \hat{z} \end{pmatrix}$

FeSe [15], MgB_2 [16], or $NbSe_2$ [17]. Indeed, the $\gamma_H(H)$ of LaPtSi exhibits a significant change in slope around $\mu_0 H = 0.2$ T, where there is a clear kink also in the $H_{c2}(T)$ data [see Supplementary Figure 5(d)]. Such field value might correspond to the critical field which suppresses the small superconducting gap. Therefore, both $\gamma_H(H)$ and $H_{c2}(T)$ change their slope around such critical field.

Supplementary Note 8

Symmetry analysis of the superconducting order parameters. The 111 materials, on the one hand appear to be fully-gapped BCS-type superconductors while, on the other hand, they show unconventional features such as the spontaneous breaking of time-reversal symmetry in the superconducting state. In general, the TRS breaking of the superconducting order parameter is required to have multiple components and a nontrivial phase difference between them [18]. We can find all the possible superconducting channels based on the analysis of normal-state symmetries within the Ginzburg-Landau theory [18, 19]. In the case of 111 materials, the corresponding point group is C_{4v}. The basis functions of the 2D irreducible representation E of C_{4v} (in the strong-SOC limit) are shown in Supplementary Table 2. Symmetry analysis indicates that there are only two symmetry-allowed time-reversal symmetry breaking superconducting channels: i) a singlet with order parameter $\Delta_0(k) = A_1(k_x + ik_y)k_z$, and ii) a triplet with an order parameter characterized by the **d**-vector given by $\mathbf{d}(k) = \left[A_2 k_z, iA_2 k_z, B_2(k_x + ik_y)\right]$. Here, $\boldsymbol{\sigma} = \{\sigma_x, \sigma_y, \sigma_z\}$ are the Pauli matrices, while A_1, A_2, and B_2 are constants independent of k. However, both these order parameters feature nodes. Hence, also a mixed-parity state resulting from these two channels will still have nodes. Note that, the nonsymmorphic symmetries present in these materials can give rise to additional nodes [20] at the Brillouin zone boundaries and zone faces. However, these cannot generate extra time-reversal symmetry breaking superconducting channels.

Thus, in 111 materials, in the single-band picture, there are no possible time-reversal symmetry breaking superconducting instabilities that are fully gapped. Hence, to account for the experimental results, we need to consider the inherent multiband nature of these materials. Incidentally, even our recent proposal of a loop-supercurrent superconducting ground state [21], applicable to some of the fully-gapped time-reversal symmetry breaking superconductors, cannot be applied to the case of 111 materials, since they have only two symmetrically distinct sites within their unit cells.

By inspecting the Fermi surfaces of these materials, we

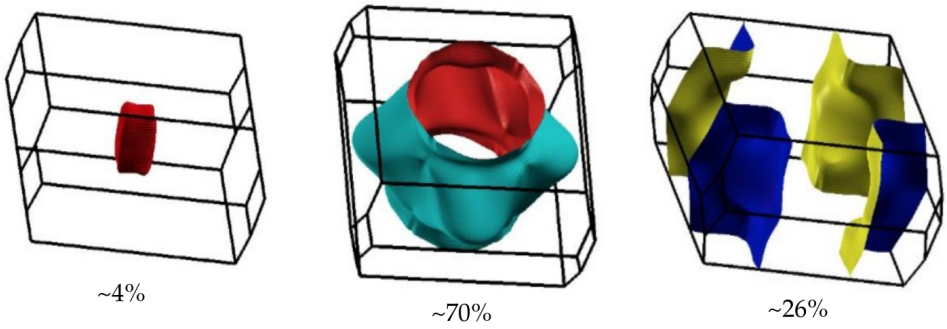

Supplementary Figure 12. Fermi surfaces of LaNiSi without SOC. The relative contributions to the density of states at the Fermi level are also shown.

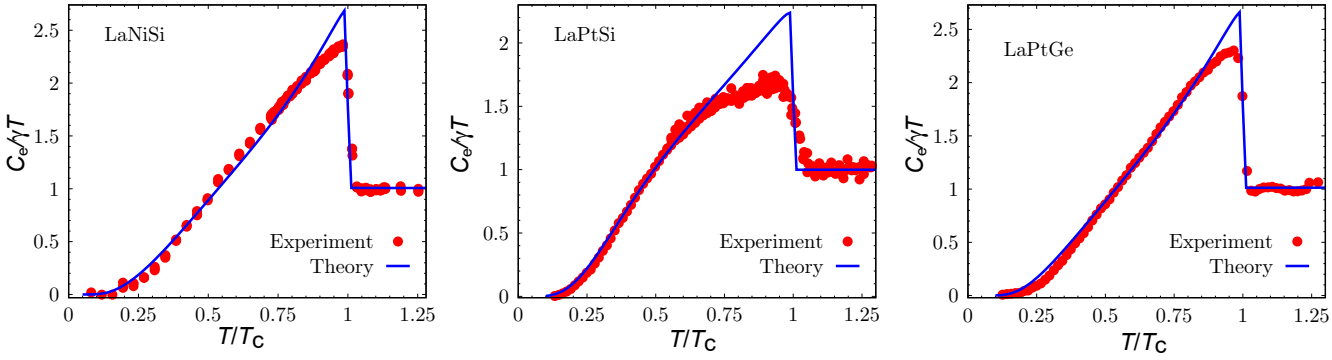

Supplementary Figure 13. Fits of experimental specific-heat data with a model considering both intra- and interband SOC. The corresponding fit parameters are given in Table S3.

note that, at all effects, they are two-band materials, whose Fermi surfaces have extensive regions within the first Brillouin zone, where they are close and parallel to each other. Hence, it is reasonable to assume that, in this case, an interband pairing is very plausible. This assumption then leads to an INT-type state, as discussed in detail in the next section.

Supplementary Note 9

Theory of internally antisymmetric nonunitary triplet pairing in the 111 materials. LaNiSi, LaPtSi, and LaPtGe share a noncentrosymmetric body-centred tetragonal crystal structure and their Fermi surfaces have the same topology. The Fermi surfaces of LaNiSi (taken from Ref. [22]) are shown in Supplementary Figure 12. Those of LaPtGe and LaPtSi were reported in Refs. [2] and [22], respectively. Only two of the three Fermi surfaces (corresponding to the second- and third Fermi surfaces of LaNiSi, shown in Supplementary Figure 12) are the most important ones, as together they contribute almost 96% to the density of states (DOS) at the Fermi level. As a result, to describe the low-energy normal-state properties of the three materials, we can effectively ignore the first Fermi surface, and work only with the second and the third Fermi surfaces. Finally, from the projected DOS it is noted that La-5d, Ni-3d, and Si-3p orbitals are the most important ones (i.e., accountig for most of the DOS at Fermi level). In LaPtSi, such orbitals are La-5d, Pt-5d, and Si-3p [2], while in LaPtGe are La-5d, Pt-5d, and Ge-4p [22].

We consider a minimal two-band model, which can qualitatively reproduce the shapes of the two most important Fermi surfaces. Then, we compute the specific heat in the internally antisymmetric nonunitary triplet (INT) state using the Bogoliubov-de-Gennes (BdG) formalism [18]. The dispersion of the two corresponding bands is given by:

$$\epsilon_1(\vec{k}) = \varepsilon_1^{(0)} + \frac{\epsilon'(\vec{k})+\epsilon''(\vec{k})}{2} - \sqrt{\left[\frac{\epsilon'(\vec{k})-\epsilon''(\vec{k})}{2}\right]^2 + t_{\rm m}^2},$$

$$\epsilon_2(\vec{k}) = \varepsilon_2^{(0)} + \frac{\epsilon'(\vec{k})+\epsilon''(\vec{k})}{2} + \sqrt{\left[\frac{\epsilon'(\vec{k})-\epsilon''(\vec{k})}{2}\right]^2 + t_{\rm m}^2},$$

$$\epsilon(k) = -2t_{\parallel}\cos(k),$$

$$\epsilon'(\vec{k}) = \frac{\epsilon(k_x)+\epsilon(k_y)}{2} - \sqrt{\left[\frac{\epsilon(k_x)-\epsilon(k_y)}{2}\right]^2 + t_\delta^2},$$

$$\epsilon''(\vec{k}) = -2t_\perp\cos(k_z) - 2t_d[\cos(k_x)+\cos(k_y)]. \qquad (2)$$

To account for the ASOC effects, phenomenologically we consider a Rashba-type SOC, as described in the text. In general, the Rashba ASOC has both an *interband* contribution of strength α,

$$V_{\rm R}^{\rm inter} = \alpha\left(k_y\sigma_x - k_x\sigma_y\right), \qquad (3)$$

and an *intraband* contribution of strength α_1

$$V_{\rm R}^{\rm intra} = \alpha_1\left(k_y\sigma_x - k_x\sigma_y\right), \qquad (4)$$

and we will be interested in the parameter regime $\alpha/\alpha_1 \ll 1$. Then the normal state Hamiltonian operator is

$$\hat{\mathscr{H}}_{\rm N} = \sum_k \hat{c}_k^\dagger \cdot H_{\rm N}(k) \cdot \hat{c}_k, \qquad (5)$$

where we define

$$\hat{c}_k = \begin{bmatrix}\tilde{c}_{\uparrow,k}\\ \tilde{c}_{\downarrow,k}\end{bmatrix} \quad \text{with} \quad \tilde{c}_{s,k} = \begin{bmatrix}c_{1,s,k}\\ c_{2,s,k}\end{bmatrix}. \qquad (6)$$

Supplementary Table 3. Fit parameters when including both inter- and intraband ASOC terms. The corresponding amplitudes of the **q**-vector are 0.030, 0.078, and 0.026 for LaNiSi, LaPtSi, and LaPtGe, respectively.

Parameter	LaNiSi	LaPtSi	LaPtGe
$\Delta_0/(k_B T_c)$	2.50	2.00	2.30
$\alpha/t_\parallel$	0.22	0.39	0.72
α_1/α	0.00005	0.00010	0.00010
$\boldsymbol{\eta}$	$\frac{1}{\sqrt{3}}\left(1, e^{0.01i\pi}, e^{1.01i\pi}\right)$	$\frac{1}{\sqrt{3}}\left(1, e^{0.01i\pi}, e^{1.03i\pi}\right)$	$\frac{1}{\sqrt{3}}\left(1, e^{0.005i\pi}, e^{1.01i\pi}\right)$

Supplementary Table 4. Fit parameters when only the interband ASOC is considered. The corresponding amplitudes of the **q**-vector are 0.030, 0.078, and 0.026 for LaNiSi, LaPtSi, and LaPtGe, respectively.

Parameter	LaNiSi	LaPtSi	LaPtGe
$\Delta_0/(k_B T_c)$	2.20	1.95	2.10
$\alpha/t_\parallel$	0.36	0.39	0.70
$\boldsymbol{\eta}$	$\frac{1}{\sqrt{3}}\left(1, e^{0.01i\pi}, e^{1.01i\pi}\right)$	$\frac{1}{\sqrt{3}}\left(1, e^{0.01i\pi}, e^{1.03i\pi}\right)$	$\frac{1}{\sqrt{3}}\left(1, e^{0.005i\pi}, e^{1.01i\pi}\right)$

Here, $c_{m,s,k}$ is an electron annihilation operator in the band $m = 1, 2$ with spin $s = \uparrow, \downarrow$. The normal-state Hamiltonian matrix is given by

$$H_N(k) = \sigma_0 \otimes \begin{bmatrix} \xi_1(k) & 0 \\ 0 & \xi_2(k) \end{bmatrix} + (k_y\sigma_x - k_x\sigma_y) \otimes (\alpha\tau_x + \alpha_1\tau_0), \tag{7}$$

where $\xi_m(k) = [\epsilon_m(k) - \mu]$, with μ being the chemical potential and σ_0 and τ_0 the identity matrices in the spin- and band spaces respectively.

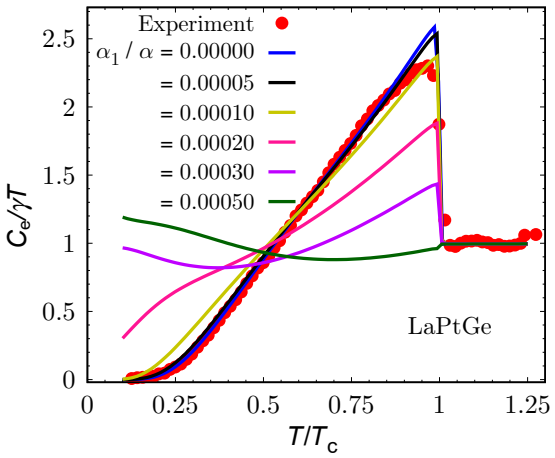

Supplementary Figure 14. Effect of changing α_1 in the LaPtGe case. The parameters are: $\alpha/t_\parallel = 0.70$, $\Delta_0/(k_B T_c) = 2.1$, $\boldsymbol{\eta} = \frac{1}{\sqrt{3}}\left(1, e^{0.005i\pi}, e^{1.01i\pi}\right)$, with normal-state parameters corresponding to Fig. 3 in the main text.

The interaction Hamiltonian in the INT channel is

$$\hat{\mathscr{H}}_{\rm INT} = \frac{1}{2}\sum_k \left[\hat{c}^\dagger_k \cdot \hat{\Delta} \cdot \hat{c}^{\dagger \rm T}_{-k} + \text{h.c.}\right], \tag{8}$$

with the pairing potential in the INT state given by

$$\hat{\Delta} = \Delta_0(\boldsymbol{\eta}\cdot\vec{\sigma})i\sigma_y \otimes i\,\tau_y, \tag{9}$$

with Δ_0 being the pairing amplitude.

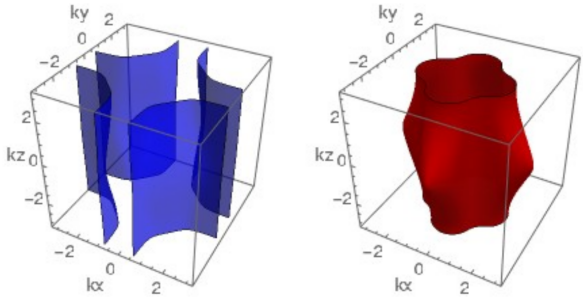

Supplementary Figure 15. Tuning the minimal-model parameters to get different Fermi-surface shapes with the same topology. The parameters are: $t_\parallel = 1$ eV, $\mu/t_\parallel = -1.5$, $t_\perp/t_\parallel = 0.85$, $t_d/t_\parallel = 3.0$, $t_\delta/t_\parallel = 0.6$, $t_m/t_\parallel = 0.4$, $\varepsilon_1^{(0)}/t_\parallel = 0.2$, and $\varepsilon_2^{(0)}/t_\parallel = 0.0$.

Then, the BdG Hamiltonian operator is

$$\begin{aligned}\hat{\mathscr{H}}_{\rm BdG} &= \hat{\mathscr{H}}_{\rm N} + \hat{\mathscr{H}}_{\rm INT} \\ &= \frac{1}{2}\sum_k \Psi_k^\dagger H_{\rm BdG}(k)\Psi_k + \text{constant},\end{aligned} \tag{10}$$

with the Nambu operators defined as

$$\Psi_k = \begin{bmatrix} \hat{c}_k \\ \hat{c}^{\dagger \rm T}_{-k} \end{bmatrix}, \tag{11}$$

and the BdG Hamiltonian matrix given by

$$H_{\rm BdG}(k) = \begin{bmatrix} H_N(k) & \hat{\Delta} \\ \hat{\Delta}^\dagger & -H_N(-k)^T \end{bmatrix}. \tag{12}$$

$H_{\rm BdG}(k)$ is diagonalized to obtain the Bogoliubov energy bands $E_n(k)$, $n = 1 \ldots 4$, which are used to compute the specific heat using the formula

$$C = \sum_{n,k} \frac{1}{2} k_B \beta^2 \left\{E_n(k) + \beta \frac{\partial E_n(k)}{\partial \beta}\right\} E_n(k)\,\text{sech}^2\left[\beta E_n(k)/2\right], \tag{13}$$

where $\beta = (k_B T)^{-1}$ and k_B is the Boltzmann constant. As described in the main text, the temperature dependence in

the quasiparticle energy bands is assumed to come only from the pairing amplitude, here described by

$$\Delta(T) = \Delta_0 \tanh\{1.82[1.018(T_c/T-1)]^{0.51}\} \qquad (14)$$

ignoring any weak temperature dependence in the **q**-vector.

To reproduce the specific-heat data, first we fix the T_c of a particular material using the experimental value and then treat $\Delta_0/(k_B T_c)$, $\boldsymbol{\eta}$, α/t, and α_1/α as general fit parameters. However, we can only fit the experimental data in the $\alpha_1/\alpha \ll 1$ limit, i.e., of a dominant interband SOC, as seen in the example shown in Supplementary Figure 13, with the corresponding fit parameters given in Supplementary Table 3. This choice is dictated by the fact that only in this limit the Fermi surfaces are not signficantly affected by the SOC, hence, their shapes remain qualitatively the same. To clarify this point, the effect of changing α_1 in the $\alpha_1/\alpha \ll 1$ regime is shown Supplementary Figure 14. For simplicity, we only consider the $\alpha_1 = 0$ case in the main text. The fit parameters for the $\alpha_1 = 0$ case are shown in Supplementary Table 4. From both Supplementary Table 3 and Table 4, we note that the trend of increasing ASOC (from LaNiSi to LaPtSi to LaPtGe) arises naturally from fits in the weak-coupling limit and we do not have to enforce it by hand. Note, however, that this is a phenomenological theory. Hence, one should refrain from making quantitative comparisons with actual material-dependent parameters, such as the ASOC strengths computed from first principles.

In absence of an intraband SOC ($\alpha_1 = 0$), the normal-state bands remain two-fold degenerate and the two degenerate Fermi surfaces with interband SOC are pushed away from each other with increasing α. Hence, for a "large" α value we are only left with one of the Fermi surfaces. To have the two Fermi surfaces remain qualitatively the same, even in presence of an interband SOC, we need to work in the $\alpha/t_{\parallel} < 0.95$ regime. By changing the hopping parameters in the minimal model described above, we can tune the shapes of the Fermi surfaces to resemble those of the respective materials. For instance, the two Fermi surfaces of LaPtGe look slightly different from those of LaNiSi. In Supplementary Figure 15, we show an example of tuning the shapes of the Fermi surfaces to make them similar to that of LaPtGe [22]. In this case, in the weak-coupling limit, we can also fit the specific-heat data quite well by tuning the SOC strengths and the direction of the nonunitary **d**-vector. Therefore, our theory is rather robust in reproducing the key features of the specific-heat curves, provided the overall topology of the Fermi surfaces remains the same.

Finally, to determine the goodness of the fits presented in Fig. 6 of the main text, we computed the coefficient of determination, denoted by R^2. For a dataset of N values, marked by y_1, ..., y_N, each associated with a fitted value f_1, ..., f_N, respectively, R^2 is defined as

$$R^2 = \left(1 - \frac{X}{Y}\right), \text{ with } \quad X = \sum_{i=1}^{N}(y_i - f_i)^2, \; Y = \sum_{i=1}^{N}(y_i - y_a)^2. \qquad (15)$$

Here, $y_a = 1/N \sum_{i=1}^{N} y_i$ is the average y value. The best fit, which matches exactly the experimental data, corresponds to R^2 equal to 1. We find that, for the fits presented in Fig. 6 of the main text, the R^2 values for LaNiSi, LaPtSi, and LaPtGe are 0.982, 0.762, and 0.985, respectively. In conjunction with the residual plots, the obtained R^2 values suggest that the fits are better for the LaNiSi and LaPtGe case than for LaPtSi. Most likely this is due to the broadening of transition in the LaPtSi case.

Supplementary Table 5. Normal-state and superconducting properties of 111 materials, as determined from electrical-resistivity, magnetic-susceptibility, specific-heat, and μSR measurements.

Property	Unit	LaNiSi	LaPtSi	LaPtGe
$T_c(\chi)$	K	1.28	3.62	3.46
$T_c(C/T)$	K	1.25	3.50	3.25
$T_c(\rho)$	K	1.25	3.50	3.30
$T_c(\mu$SR)	K	1.10	3.40	3.15
$\mu_0 H_{c1}(0)$	mT	3.9(5)	9.6(2)	11.8(1)
$\mu_0 H_{c1}(0)$[a]	mT	5.6(2)	8.6(2)	7.6(2)
$\mu_0 H_{c2}(0)$	T	0.10(1)	1.17(2)	0.44(1)
$\xi(0)$	nm	57(2)	17(1)	27(1)
κ ($\equiv \lambda/\xi$)	—	3.5	13.4	8.1
ρ_0	$\mu\Omega$cm	18	62	66
γ_n	mJ/mol-K^2	9.06(17)	6.20(10)	6.55(20)
β	mJ/mol-K^4	0.273(63)	0.392(3)	0.642(6)
$\Delta_0(\mu$SR)[b]	$k_B T_c$	1.95(5)	1.80(5)	2.10(5)
$\Delta_0(\mu$SR)[c]	$k_B T_c$	1.90(5)	1.65(5)	1.90(5)
$\Delta_0(C/T)$	$k_B T_c$	2.20(5)	1.95(5)	2.10(5)
$\Delta C/\gamma T_c$	—	1.38	0.73[d]	1.34
λ_0	nm	300(3)	228(3)	219(2)
$\lambda_{GL}(0)$[a]	nm	260(20)	213(3)	163(2)
Λ_{ZF}[e]	μs^{-1}	0.0277(9)	0.030(1)	0.0202(9)
σ_{ZF}[f]	μs^{-1}	0.0938(38)	0.1026(50)	0.1038(33)
l_e	nm	32.3(3)	8.9(1)	7.8(1)
ξ_0	nm	51(1)	33(3)	31(1)
ξ_0/l_e	–	1.58	3.71	3.97
$m^\star$	m_e	10.3(1)	6.4(1)	6.4(1)
n_s	10^{27} m^{-3}	3.23(4)	3.49(4)	3.75(4)
v_F	10^4 ms^{-1}	5.14(5)	8.45(7)	8.7(2)
T_F	10^3 K	0.90(1)	1.51(1)	1.60(4)

[a] Calculated by $\mu_0 H_{c1} = (\Phi_0/4\pi\lambda^2)[\ln(\kappa) + 0.12]$.
[b] Clean-limit model.
[c] Dirty-limit model.
[d] The reduced value is due to the broad superconducting transition.
[e] Λ_{ZF} value at base temperature.
[f] Average value.

Supplementary Note 10

Uemura plot. We now compare the superconducting parameters of 111 materials with those of other TRS-breaking superconductors. By using the parameters derived here from the electrical resistivity-, magnetization-, heat capacity-, and μSR measurements, the effective mass $m^\star$, carrier density n_s, BCS coherence length ξ_0, electronic mean-free path l_e, Fermi velocity v_F, and effective Fermi temperature T_F could be estimated following the methods reported in Ref. 27. All these parameters are summarized in Supplementary Table 5. The calculated Fermi temperatures are $T_F = 0.9 \times 10^3$, 1.51×10^3, and 1.60×10^3 K for LaNiSi, LaPtSi, and LaPtGe, respectively. T_F is proportional to $n_s^{2/3} m^{\star -1}$, where n_s and $m^\star$ are the carrier density and the effective mass. Consequently, the different families of superconductors can be classified according to their T_c/T_F ratios into a so-called Uemura plot [29]. Several types of unconventional superconductors, including heavy fermions, organics, high-T_c iron pnictides, and cuprates, all lie in a $10^{-2} < T_c/T_F < 10^{-1}$ band (gray

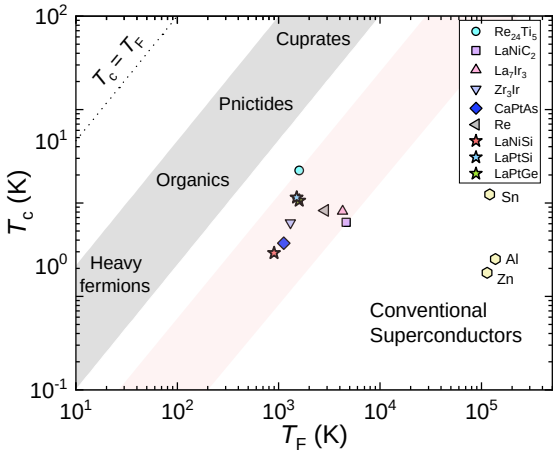

Supplementary Figure 16. Uemura plot showing the superconducting transition T_c vs the effective Fermi temperature T_F for different types of superconductors. The grey-shaded region, with $1/100 < T_c/T_F < 1/10$, indicates the band of unconventional superconductors, such as heavy fermions, organics, fullerenes, pnictides, cuprates. The red-shaded region marks the T_c/T_F value between 4.8×10^{-4} and 3.6×10^{-3}, where many different types of superconductors with broken TRS are located, including the 111 materials studied here, as well as others, such as $Re_{24}Ti_5$, $LaNiC_2$, La_7Ir_3, Zr_3Ir, CaPtAs, and elementary rhenium. The dotted line corresponds to $T_c = T_F$. The data of the reference samples were adapted from Refs. [12, 23–28].

region in Fig. SSupplementary Figure 16). Conversely, most of conventional superconductors, such as Al, Sn, and Zn, are located at $T_c/T_F \lesssim 10^{-4}$. Between these two classes lie several superconductors known to break TRS below the onset of T_c (see red-shaded region), including the noncentrosymmetric $Re_{24}Ti_5$, $LaNiC_2$, La_7Ir_3, Zr_3Ir, and CaPtAs [23–26, 28], and centrosymmetric elementary rhenium [12, 27]. For LaNiSi, $T_c/T_F = 1.4 \times 10^{-3}$ is almost identical to the analogous value for CaPtAs ($T_c/T_F = 1.3 \times 10^{-3}$), the latter representing a rare NCSC that simultaneously breaks TRS and exhibits superconducting gap nodes [28]. While for LaPtSi and LaPtGe, the $T_c/T_F = 2$–2.3×10^{-3} is located between Zr_3Ir ($T_c/T_F = 1.7 \times 10^{-3}$) and the α-Mn-type $Re_{24}Ti_5$ ($T_c/T_F = 3.6 \times 10^{-3}$), both of which exhibit broken TRS and a fully-gapped superconducting state, similar to the 111 materials. Clearly, the 111 materials studied here lie in the TRS-breaking band in the Uemura plot.

Supplementary References

1. Lee, W. H., Yang, F. A., Shih, C. R. & Yang, H. D. Crystal structure and superconductivity in the Ni-based ternary compound LaNiSi. *Phys. Rev. B* **50**, 6523–6525 (1994).
2. Kneidinger, F. *et al.* Synthesis, characterization, electronic structure, and phonon properties of the noncentrosymmetric superconductor LaPtSi. *Phys. Rev. B* **88**, 104508 (2013).
3. Evers, J., Oehlinger, G., Weiss, A. & Probst, C. Supraconductivity of LaPtSi and LaPtGe. *Solid State Commun.* **50**, 61–62 (1984).
4. Canepa, F., Cirafici, S., Merlo, F. & Palenzona, A. Electrical resistivity in the R_5S_3 systems (R = La, Ce, Pr, Nd, Sm). *J. Alloys Compd.* **203**, L11–L13 (1994).
5. Werthamer, N. R., Helfand, E. & Hohenberg, P. C. Temperature and purity dependence of the superconducting critical field, H_{c2}. III. Electron spin and spin-orbit effects. *Phys. Rev.* **147**, 295–302 (1966).
6. Gurevich, A. Enhancement of the upper critical field by nonmagnetic impurities in dirty two-gap superconductors. *Phys. Rev. B* **67**, 184515 (2003).
7. Brandt, E. H. Properties of the ideal Ginzburg-Landau vortex lattice. *Phys. Rev. B* **68**, 054506 (2003).
8. Sajilesh, K. P., Singh, D., Biswas, P. K., Hillier, A. D. & Singh, R. P. Superconducting properties of the noncentrosymmetric superconductor LaPtGe. *Phys. Rev. B* **98**, 214505 (2018).
9. Sajilesh, K. P., Singh, D., Hillier, A. D. & Singh, R. P. Probing nodeless superconductivity in LaMSi (M = Ni, Pt) using muon-spin rotation and relaxation. *Phys. Rev. B* **102**, 094515 (2020).
10. Tinkham, M. *Introduction to Superconductivity* (Dover Publications, Mineola, NY, 1996), 2 edn.
11. Tari, A. *The Specific Heat of Matter at Low Temperatures* (Imperial College Press, London, 2003).
12. Shang, T. *et al.* Time-reversal symmetry breaking in Re-based superconductors. *Phys. Rev. Lett.* **121**, 257002 (2018).
13. Volovik, G. E. Superconductivity with lines of gap nodes: density of states in the vortex. *JETP Lett.* **58**, 469–473 (1993).
14. Wen, H.-H. *et al.* Electronic specific heat and low-energy quasiparticle excitations in the superconducting state of $La_{2-x}Sr_xCuO_4$ single crystals. *Phys. Rev. B* **70**, 214505 (2004).
15. Chen, J. T., Sun, Y., Yamada, T., Pyon, S. & Tamegai, T. Two-gap features revealed by specific heat measurements in FeSe. *J. Phys. Conf. Ser.* **871**, 012016 (2017).
16. Bouquet, F., Fisher, R. A., Phillips, N. E., Hinks, D. G. & Jorgensen, J. D. Specific heat of $Mg^{11}B_2$: Evidence for a second energy gap. *Phys. Rev. Lett.* **87**, 047001 (2001).
17. Huang, C. L. *et al.* Experimental evidence for a two-gap structure of superconducting $NbSe_2$: A specific-heat study in external magnetic fields. *Phys. Rev. B* **76**, 212504 (2007).
18. Ghosh, S. K. *et al.* Recent progress on superconductors with time-reversal symmetry breaking. *J. Phys: Cond. Matt.* **33**, 033001 (2020).
19. Sigrist, M. & Ueda, K. Phenomenological theory of unconventional superconductivity. *Rev. Mod. Phys.* **63**, 239–311 (1991).
20. Sumita, S. & Yanase, Y. Unconventional superconducting gap structure protected by space group symmetry. *Phys. Rev. B* **97**, 134512 (2018).
21. Ghosh, S. K., Annett, J. F. & Quintanilla, J. Time-reversal symmetry breaking in superconductors through loop supercurrent order. *New J. Phys.* **23**, 083018 (2021).
22. Zhang, P., Yuan, H. & Cao, C. Electron-phonon coupling and nontrivial band topology in noncentrosymmetric superconductors LaNiSi, LaPtSi, and LaPtGe. *Phys. Rev. B* **101**, 245145 (2020).
23. Shang, T. *et al.* Nodeless superconductivity and time-reversal symmetry breaking in the noncentrosymmetric superconductor $Re_{24}Ti_5$. *Phys. Rev. B* **97**, 020502 (2018).
24. Shang, T. *et al.* Time-reversal symmetry breaking in the noncentrosymmetric Zr_3Ir superconductor. *Phys. Rev. B* **102**, 020503(R) (2020).
25. Hillier, A. D., Quintanilla, J. & Cywinski, R. Evidence for time-reversal symmetry breaking in the noncentrosymmetric superconductor $LaNiC_2$. *Phys. Rev. Lett.* **102**, 117007 (2009).
26. Barker, J. A. T. *et al.* Unconventional superconductivity in La_7Ir_3 revealed by muon spin relaxation: Introducing a new family of noncentrosymmetric superconductor that breaks time-reversal symmetry. *Phys. Rev. Lett.* **115**, 267001 (2015).
27. Shang, T. *et al.* $Re_{1-x}Mo_x$ as an ideal test case of time-reversal symmetry breaking in unconventional superconductors. *npj Quantum Mater.* **5**, 76 (2020).
28. Shang, T. *et al.* Simultaneous nodal superconductivity and time-reversal symmetry breaking in the noncentrosymmetric superconductor CaPtAs. *Phys. Rev. Lett.* **124**, 207001 (2020).
29. Uemura, Y. J. *et al.* Basic similarities among cuprate, bismuthate, organic, Chevrel-phase, and heavy-fermion superconductors shown by penetration-depth measurements. *Phys. Rev. Lett.* **66**, 2665 (1991).